


# Afterbody Curvature Effects on Flow Loss Characteristics Based on Entropy Production

Xinwei Chen[1], Miaosheng He[1], Bin Yu[1], Wei Wang[1], Hong Liu[1]

[1]Shanghai Jiao Tong University, School of Aeronautics and Astronautics, Hypersonic Innovation Technology Laboratory, Shanghai, 200240, China

## Abstract

Afterbody curvature is an important geometric parameter for high-speed aircraft because it can simultaneously affect pressure recovery, wall-shear distribution, wake development, and irreversible flow loss. In this study, a two-dimensional wide-range-speed aircraft profile is investigated using steady compressible Reynolds-averaged Navier-Stokes (RANS) simulations and an entropy-production-based loss analysis framework. The afterbody curvature is parameterized by the tail curvature radius, with three cases considered at $Ma_\infty = 6$: $R_{tail} / R_{tail,st} = 0.75, 1.00, 1.25$. The surface drag is decomposed into pressure and viscous contributions, while the entropy-production loss is decomposed by geometric region and flow structure. Results show that increasing $R_{tail}$ reduces the tail pressure drag but increases the tail viscous drag. Consequently, the total drag changes only weakly because of compensation between these two components. Surface-pressure distributions indicate that afterbody curvature modifies the pressure-recovery process, whereas skin-friction data show that the increase in viscous drag is mainly associated with the increasing afterbody arc length rather than an increase in the mean skin-friction level. Entropy-production analysis further shows that the high-entropy regions remain in similar locations, but their intensity varies with curvature. The results demonstrate that afterbody curvature affects drag through coupled pressure and viscous pathways, and that entropy production provides complementary information for interpreting local loss-generation mechanisms.

**Keywords:** Entropy production, Near-field drag decomposition, Flow loss decomposition, Tail curvature radius

## 1. Introduction

High-speed aircraft configurations often experience complex aerodynamic losses caused by the coexistence and interaction of shock waves, boundary layers, and wakes. For such configurations, afterbody shaping is especially important because the afterbody controls the pressure-recovery process after the shock, the downstream wake, and the surface area exposed to viscous stress. Therefore, even a modest geometric modification near the tail may alter both the pressure-force component and the viscous-force component of drag.

Previous investigations of boattail and afterbody geometries have shown that afterbody contour, boattail angle, and curvature can have a pronounced influence on pressure distribution, separation behavior, and axial force [1-4]. In particular, increasing the radius of curvature or adopting a smoother circular-arc-type afterbody can reduce afterbody axial-force or drag under certain operating conditions [1,2]. These studies indicate that afterbody curvature is not simply a geometric detail, but a parameter that can affect the balance between pressure recovery, viscous effects, and wake development.

For high-speed flows, however, total drag alone is insufficient for identifying the mechanism of curvature-induced change. Aerodynamic drag consists of pressure drag and viscous drag, and these two components may respond differently to afterbody curvature. A larger tail curvature radius may smooth the afterbody contour and modify pressure recovery, thereby reducing pressure drag. At the same time, it may increase the afterbody arc length and the wall area over which viscous stress acts, thereby increasing viscous drag. Consequently, a small change in total drag may conceal a clear redistribution between pressure and viscous contributions. Therefore, a component-resolved drag analysis is necessary for clarifying the role of afterbody curvature.

In addition to the force-based drag decomposition, thermodynamic entropy production provides a field-based way to quantify irreversible loss generation. Entropy production has been widely used to assess energy loss and local irreversibility in thermal-fluid systems [5-8]. In compressible flows, entropy can be generated in shock waves, boundary layers, and wakes through heat conduction and viscous dissipation. Such a field-based method is valuable because it links the magnitude of loss to the spatial source of irreversibility. Preliminary entropy-production analyses of wide-range-speed flow loss suggested that the loss distribution reorganizes with Mach number and that an additional entropy-producing region may appear near the curved afterbody in high-supersonic and hypersonic regimes. This observation motivates a more detailed mechanism-level study of the afterbody neighborhood.

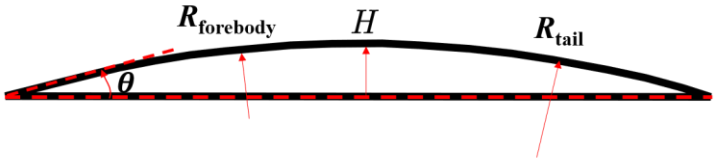
The objective of the present paper is to clarify how afterbody curvature changes aerodynamic drag and entropy-production loss for a two-dimensional wide-range-speed aircraft profile at $Ma_\infty = 6$. Three tail curvature radii are considered while the forebody and main-body geometry are kept fixed. The analysis aims to answer four questions: (i) how does the tail curvature radius affect the total drag; (ii) whether the drag change is dominated by pressure drag or viscous drag; (iii) whether the drag trend is consistent with the entropy-production loss trend; and (iv) how curvature modifies the flow structure, surface pressure, skin friction, and regional entropy production. By combining drag decomposition with entropy-production analysis, the present work provides a mechanism-oriented interpretation of curvature-induced drag variation in the afterbody region.

## 2. Methods

### 2.1 Geometry and Case Setup

A generic two-dimensional body profile is used to represent the main aerodynamic features of a wide-range-speed aircraft fuselage, as shown in Fig. 1. This representative longitudinal body geometry captures the essential forebody compression, afterbody pressure recovery, wall-shear contribution, and wake development of a wide-range-speed aircraft. The afterbody is re-parameterized using the tail curvature radius $R_{tail}$. The forebody geometry is fixed for all curvature cases, with the leading-edge angle $\theta = 15^\circ$, forebody curvature radius $R_{forebody} = 557\text{mm}$, and height $H = 25\text{mm}$. Only the afterbody curvature is modified. The standard tail curvature radius is denoted as $R_{tail,st} = 557\text{mm}$, and three curvature cases are considered:

$$R_{tail} / R_{tail,st} = 0.75, 1.00, 1.25 \tag{1}$$




$\boldsymbol{\theta}$: leading-edge angle, typically selected within 10° to 20° for slender high-speed profiles.

$\boldsymbol{R_{forebody}}$ : forebody curvature radius, constrained by the effective height of the wind-tunnel test section and the allowable blockage ratio.

$H$ : profile height, also constrained by the effective height of the wind-tunnel test section and the allowable blockage ratio.

$\boldsymbol{R_{tail}}$ : defined relative to the forebody curvature radius. In this study, $R_{tail}$ is varied within 0.75-1.25 $R_{forebody}$.

Figure 1 – Generic two-dimensional body profile and geometric parameters used to represent the longitudinal aerodynamic features of a wide-range-speed aircraft fuselage.

The afterbody-curvature study is conducted at $Ma_\infty = 6$, where the flow loss is expected to be strongly affected by shock-related irreversibility. The freestream dynamic pressure is approximately $q_\infty = 46\text{kPa}$. The reference depth is set to 1 m, and the drag values are reported in Newtons.

The freestream static pressure $P_\infty$ is obtained from the specified dynamic pressure using

$$q_\infty = \frac{1}{2}\gamma P_\infty Ma_\infty^2 \tag{2}$$

and the freestream density $\rho_\infty$ and velocity are determined from

$$P_\infty = \rho_\infty R T_\infty \tag{3}$$

$$U_\infty = Ma_\infty \sqrt{\gamma R T_\infty} \tag{4}$$

## 2.2 Numerical Method

The flow field is computed using ANSYS Fluent. The governing equations are the two-dimensional steady compressible Reynolds-averaged Navier-Stokes equations, which can be written in conservative form as

$$\frac{\partial \mathbf{F}_i}{\partial x_i} - \frac{\partial \mathbf{F}_v}{\partial x_i} = 0 \tag{5}$$

where the inviscid flux vector is

$$\mathbf{F}_i = \left[ \rho u_i \quad \rho u u_i + p\delta_{1i} \quad \rho v u_i + p\delta_{2i} \quad (\rho E + p) u_i \right]^T \tag{6}$$

and the viscous flux vector is

$$\mathbf{F}_v = \left[ 0 \quad \tau_{1i} \quad \tau_{2i} \quad u_j \tau_{ji} - q_i \right]^T \tag{7}$$

Here, $\rho$ is the density, $u$ and $v$ are the velocity components, $p$ is the static pressure, $E$ is the total energy per unit mass, $\delta_{ij}$ is the Kronecker delta, $\tau_{ij}$ is the viscous stress tensor, and $q_i$ is the heat flux. Turbulence closure is provided by the $k-\omega$ SST model. The density-based implicit formulation is used. Roe-type flux splitting and second-order upwind discretization are adopted for the convective terms. Air is treated as an ideal gas with constant specific heat ratio $\gamma = 1.4$ and specific heat $C_p = 1006.43 \, \mathrm{J/(kg \cdot K)}$. The dynamic viscosity is evaluated using Sutherland's law, and the Prandtl number used in the entropy-production calculation is $\mathrm{Pr} = 0.85$.

The computational domain extends approximately 0.366m upstream and 0.365m downstream of the profile reference origin, with a vertical height of 0.25m. As shown in Fig. 2, the inlet boundary is specified as a pressure inlet. The lower boundary is treated as a symmetry boundary, while the upper and downstream boundaries are specified as pressure outlets. The aircraft profile surface is treated as a no-slip adiabatic wall. The residuals of all solved variables are reduced below $10^{-3}$, and the lift and drag force coefficients are monitored to ensure a stable converged solution.

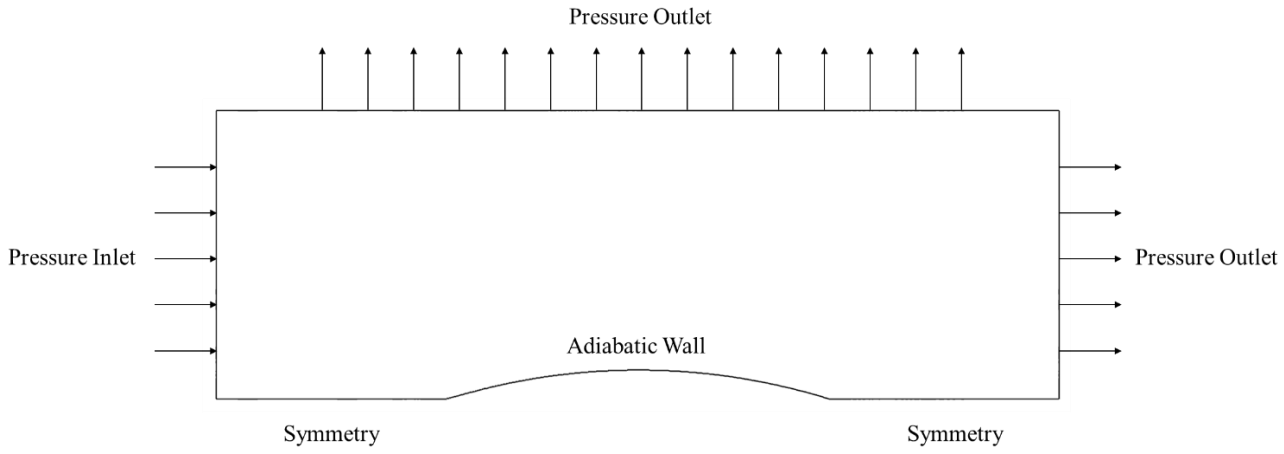



Figure 2 – Computational domain and boundary conditions.

## 2.3 Drag Decomposition

The total drag $D$ is decomposed into pressure drag $D_p$ and viscous drag $D_f$:

$$D = D_p + D_f \tag{8}$$

The pressure drag is obtained by integrating the streamwise component of the pressure force over the wall surface:

$$D_p = -\int_{S_w} (p - p_\infty) n_x \, \mathrm{d}S \tag{9}$$

where $n_x$ is the streamwise component of the outward wall-normal vector, and $S_w$ denotes the wall surface. The viscous drag is obtained from the streamwise component of the wall shear force:

$$D_f = \int_{S_w} (\boldsymbol{\tau} \cdot \mathbf{n}) \cdot \mathbf{e}_x \mathrm{d}S \tag{10}$$

where $\boldsymbol{\tau}$ is the viscous stress tensor, $\mathbf{n}$ is the wall-normal vector, and $\mathbf{e}_x$ is the unit vector in the streamwise direction. The force integration is performed separately over the forebody, tail, and entire profile. Because the reference depth is 1 m in the two-dimensional computation, the reported drag values are interpreted as drag forces for a unit-depth configuration.

To interpret the pressure-drag mechanism, the pressure coefficient distribution over the wall is examined:

$$C_p = \frac{p - p_\infty}{q_\infty} \tag{11}$$

Similarly, the skin-friction coefficient $C_f$ is used to examine the viscous-drag mechanism. To distinguish the effect of local skin-friction level from that of afterbody surface length, two integral indicators are evaluated along the tail wall. The afterbody arc length is approximated as:

$$s_{tail} = \sum_i \delta_{s,i} \tag{12}$$

For the tail region, the approximate afterbody arc length $s$ is also computed from the wall coordinates:

$$\delta_{s,i} = \sqrt{(x_{i+1} - x_i)^2 + (y_{i+1} - y_i)^2} \tag{13}$$

The arc-length-averaged skin-friction coefficient is defined as:

$$\overline{C_f} = \frac{\int_{tail} C_f \mathrm{d}s}{\int_{tail} \mathrm{d}s} \approx \frac{\sum_i C_{f,i} \delta_{s,i}}{s_{tail}} \tag{14}$$

Meanwhile, the integrated skin-friction indicator

$$I_f = \int_{tail} C_f \mathrm{d}s \approx \sum_i C_{f,i} \delta_{s,i} \tag{15}$$

is used to evaluate the cumulative contribution of skin friction along the afterbody surface.

## 2.4 Entropy-Production Framework and Region Definition

The entropy production rate in a flow field arises from two mechanisms [9]: heat conduction ( $\dot{S}'''_{therm}$ ) and viscous dissipation ( $\dot{S}'''_{visc}$ ). The total entropy production rate per unit volume is given by Moore 1983 [8]:

$$\dot{S}''' = \underbrace{\frac{k}{T^2} \frac{\partial T}{\partial x_i} \frac{\partial T}{\partial x_i}}_{\dot{S}'''_{therm}} + \underbrace{\frac{2\mu s_{ij} s_{ij}}{T}}_{\dot{S}'''_{visc}} \tag{16}$$

where $k$ is the heat conduction coefficient, $T$ is the temperature, $\mu$ is the dynamic viscosity, and $s$ is the strain-rate tensor. The heat conduction coefficient is defined as:

$$k = \frac{C_p \mu}{\mathrm{Pr}} \tag{17}$$

Here, $C_p$ denotes the specific heat at constant pressure. The entropy production loss is calculated as:

$$Loss = \iiint_\Omega \dot{S}''' T_0 \mathrm{d}V \tag{18}$$

where $T_0$ is the freestream temperature, and $\Omega$ is the region of interest.

Two types of regional decomposition are used. First, a geometric decomposition separates the flow field into a forebody-dominated region and an afterbody-neighborhood region. The afterbody-neighborhood region is defined as the region satisfying $x \geq 0$ and $\eta = \frac{y - y_{sym}}{H} \leq 1.5$, where $y_{sym}$

denotes the *y*-coordinate of the symmetry boundary. This definition encloses the afterbody boundary-layer region and near wake. The remaining part of the domain is treated as the forebody-dominated region. This definition is used to quantify how much irreversibility is locally associated with the afterbody neighborhood.

Second, a flow-structure-based decomposition is used to distinguish shock-dominated, boundary-layer-dominated, and wake-dominated losses. The boundary-layer-dominated region is identified using the *Q*-criterion (*Q*>0) within the afterbody-neighborhood range ( $x_{LE} < x < x_{TE}$ and $\eta \le 1.5$, where $x_{LE}$ and $x_{TE}$ are the streamwise coordinates of the leading edge and tail end of the aircraft profile). The wake-dominated region is further defined as $x > x_{TE}$ and $\eta \le 1.5$. The shock surface is first identified using the pressure-gradient-based criteria proposed by Xu [10], which involve satisfying both Eq. (19) and Eq. (20):

$$Ma_n = \frac{\mathbf{V} \cdot \nabla p}{a|\nabla p|} \ge K_s \tag{19}$$

$$|\nabla p| \ge \varepsilon \frac{p}{l_n} \tag{20}$$

In these equations, $Ma_n$ denotes the normal Mach number ahead of the shock wave, $\mathbf{V}$ is the velocity vector, $p$ represents the pressure, $a$ is the local speed of sound, $K_s$ is a threshold parameter for shock detection, $\varepsilon$ is a filter factor, and $l_n$ denotes the mesh size in the flow direction. Equation (19) ensures that the flow ahead of the shock is supersonic, while Equation (20) identifies regions with strong local pressure gradients characteristic of shock waves. In this study, $K_s$ is set to 0.8, and $\varepsilon$ is chosen as 0.01. The shock surface is defined as the intersection of the regions satisfying both criteria. However, the detected shock surface represents only a thin discontinuity, whereas entropy production is distributed over a broader shock-affected compression region. Therefore, for the regional entropy-production integration, the boundary-layer-dominated and wake-dominated regions are first excluded, and the remaining high-entropy-production region is treated as the shock-dominated region. This practical definition is applied consistently to all curvature cases for trend comparison.

## 3. Results and Discussion

### 3.1 Overall Flow-Field Structure Under Afterbody-Curvature Variation

At $Ma_\infty = 6$, the three afterbody-curvature cases exhibit broadly similar global flow topology, as shown by the Mach-number contours in Fig. 3. The main shock and wake pattern are not fundamentally altered by the moderate variation of $R_{tail}$, which indicates that the afterbody-curvature modification does not act by reorganizing the entire external flow field, but mainly by changing the local afterbody contour and the near-tail flow development.

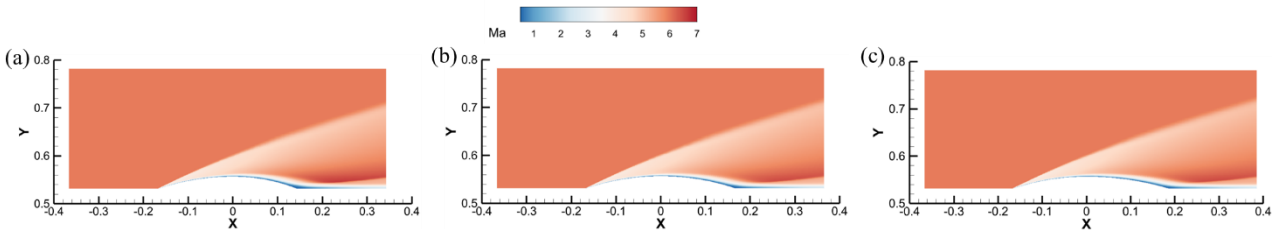



Figure 3 – Mach-number contours around the afterbody for different tail curvature radii at $Ma_\infty = 6$: (a) $R_{tail} / R_{tail,st} = 0.75$, (b) $R_{tail} / R_{tail,st} = 1.00$, and (c) $R_{tail} / R_{tail,st} = 1.25$.

### 3.2 Drag Response to Afterbody Curvature

Although the Mach-number contours suggest similar overall flow structures, as $R_{tail}$ increases, the afterbody contour becomes smoother and longer, which can modify the local pressure-recovery process and the wall-shear integration. Therefore, a force-component decomposition is required to

determine how the curvature variation affects pressure drag and viscous drag separately.

The drag decomposition for the three tail-curvature cases is summarized in Table 1 and visualized in Fig. 4. As shown in Fig. 4(a), the net drag is dominated by the pressure component for all three cases, while the viscous contribution accounts for a smaller but non-negligible portion. For the net drag, increasing $R_{tail} / R_{tail,st}$ from 0.75 to 1.25 reduces the pressure drag from 199.82 N to 197.20 N, corresponding to a decrease of approximately 1.31%. Meanwhile, the viscous drag increases from 39.38 N to 41.08 N, corresponding to an increase of approximately 4.32%. As a result, the total drag decreases only from 239.20 N to 238.28 N, a change of approximately 0.39%. This indicates that the total-drag response is weak because the pressure-drag reduction is partially compensated by the viscous-drag increase.

The compensation mechanism becomes more evident when the tail contribution is examined separately, as shown in Fig. 4(b). As $R_{tail} / R_{tail,st}$ increases from 0.75 to 1.25, the tail pressure drag decreases from 26.84 N to 24.20 N, a reduction of 9.82%. In contrast, the tail viscous drag increases from 6.54 N to 8.15 N, an increase of 24.61%. The tail total drag therefore decreases only from 33.38 N to 32.35 N, corresponding to 3.07%. This result indicates that the afterbody-curvature effect is much clearer in the component-level decomposition than in the total-drag variation alone.

Table 1 – Drag decomposition for three afterbody-curvature cases at $Ma_\infty = 6$.

| $R_{tail} / R_{tail,st}$ | Region | Pressure drag (N) | Viscous drag (N) | Total drag (N) |
|---|---|---|---|---|
| 0.75 | Forebody | 172.98 | 32.84 | 205.83 |
| | Tail | 26.84 | 6.54 | 33.38 |
| | Net | 199.82 | 39.38 | 239.20 |
| 1.00 | Forebody | 173.03 | 33.51 | 206.54 |
| | Tail | 25.34 | 7.46 | 32.80 |
| | Net | 198.37 | 40.98 | 239.34 |
| 1.25 | Forebody | 173.00 | 32.94 | 205.93 |
| | Tail | 24.20 | 8.15 | 32.35 |
| | Net | 197.20 | 41.08 | 238.28 |

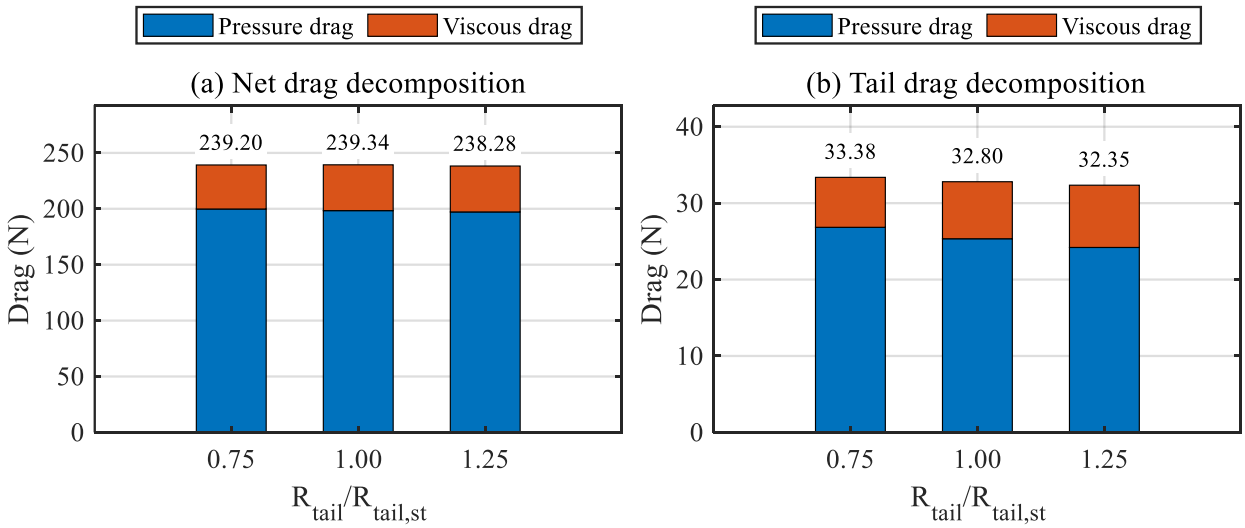



Figure 4 – Drag decomposition under afterbody-curvature variation at $Ma_\infty = 6$: (a) net pressure and viscous drag; (b) tail pressure and viscous drag. The numbers above the bars denote the corresponding total drag.

These results show that the afterbody curvature effect should not be judged only from total drag. Although the total drag varies slightly, the underlying pressure and viscous components change in opposite directions. Increasing $R_{tail} / R_{tail,st}$ weakens the pressure-drag contribution but strengthens the integrated viscous contribution. The mechanism of these two trends is discussed in the following sections.

## 3.3 Pressure-Drag Mechanism Based on Afterbody Pressure Distribution

The pressure-drag component is closely related to the pressure recovery over the afterbody and to the local surface orientation. The afterbody $C_p$ distributions for the three curvature cases are therefore compared in Fig. 5.

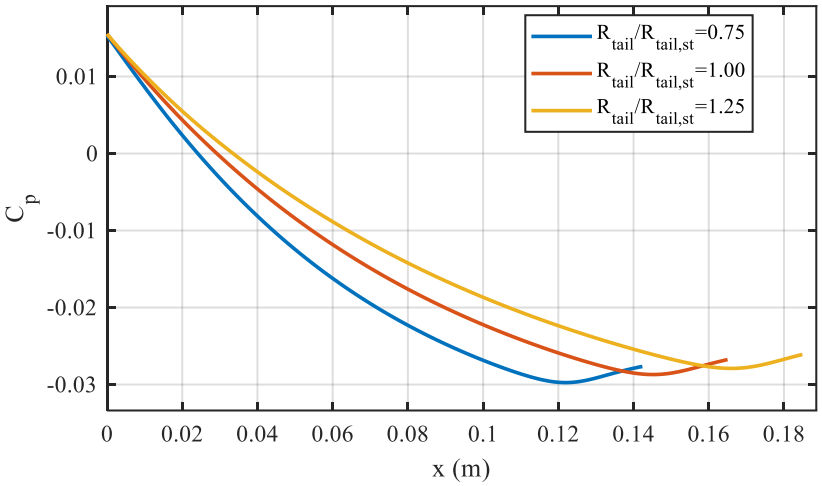



Figure 5 – Afterbody surface-pressure coefficient distribution.

The three $C_p$ curves have similar overall shapes, indicating that the afterbody pressure-recovery pattern is not fundamentally changed by the moderate curvature variation. However, the pressure level and the recovery path over the tail are still modified by $R_{tail}$. As $R_{tail}$ increases, the afterbody contour becomes smoother and the pressure distribution is redistributed along a longer tail surface. Since pressure drag depends on both the local pressure level and the wall orientation, the surface $C_p$ distribution should be interpreted together with the integrated pressure-drag data. The monotonic decrease in tail pressure drag therefore reflects the combined effect of curvature-induced pressure redistribution and the change in local surface orientation.

The corresponding near-afterbody pressure contours are shown in Fig. 6. The three cases exhibit similar overall pressure-field topology, but local differences appear near the afterbody surface and downstream recovery region. As $R_{tail}$ increases, the afterbody contour becomes smoother and the pressure variation is distributed over a longer surface, which weakens the projected pressure-force contribution in the drag direction. This is consistent with the monotonic decrease in tail pressure drag shown in Fig. 4(b).

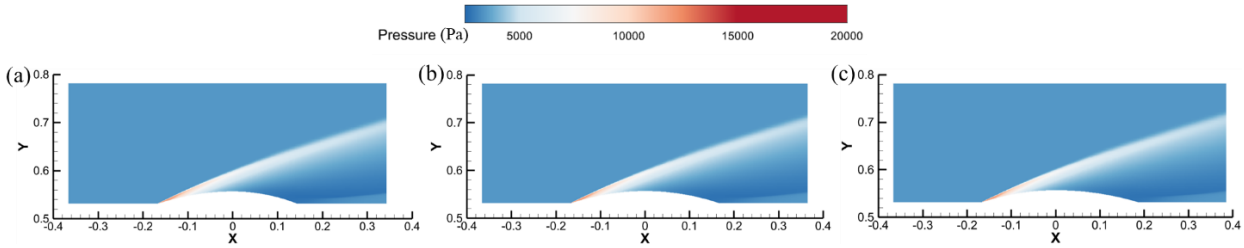



Figure 6 – Static pressure contours near the afterbody for different tail curvature radii at $Ma_\infty = 6$: (a) $R_{tail} / R_{tail,st} = 0.75$, (b) $R_{tail} / R_{tail,st} = 1.00$, and (c) $R_{tail} / R_{tail,st} = 1.25$.

## 3.4 Viscous-Drag Mechanism Based on Skin Friction and Afterbody Arc Length

The viscous-drag component increases with $R_{tail}$, especially in the tail region. To determine whether this increase is caused by a higher local wall-shear level or by a larger afterbody surface length, the afterbody $C_f$ distributions and arc lengths are examined.

The $C_f$ distributions show that the local skin-friction level over the afterbody remains of the same order for all three cases, as shown in Fig. 7. The surface-averaged skin-friction coefficient over the tail $\overline{C_f}$ does not increase with $R_{tail}$. Instead, it slightly decreases from $9.83\times10^{-4}$ for $R_{tail} / R_{tail,st} = 0.75$ to

$9.69\times10^{-4}$ for the standard case and $9.45\times10^{-4}$ for $R_{tail}/R_{tail,st}=1.25$. However, the afterbody arc length increases from 0.1453 m to 0.1871 m, as shown in Fig. 8. As a result, the integrated indicator $I_f$ increases from $1.43\times10^{-4}$ to $1.77\times10^{-4}$, as summarized in Table 2. This explains why the tail viscous drag increases despite the slight decrease in the $\overline{C_f}$.

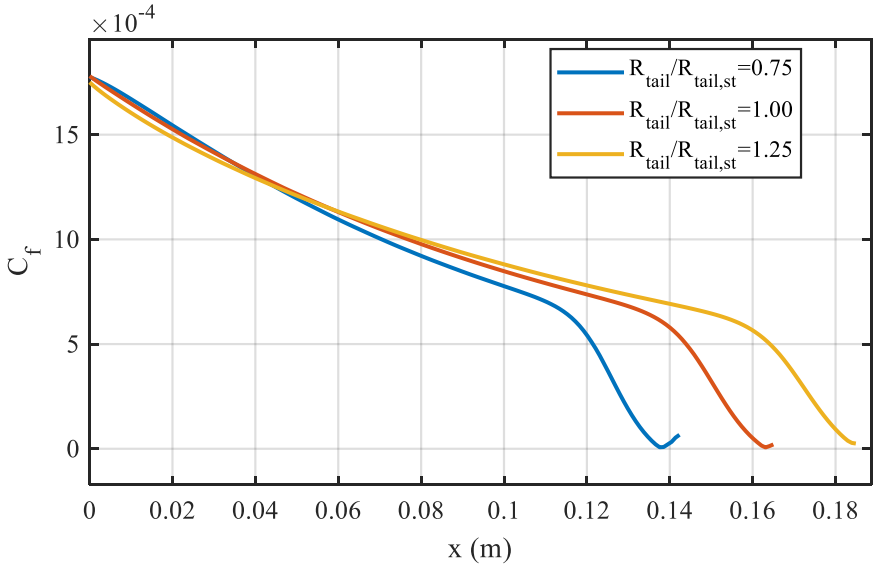



Figure 7 – Afterbody skin-friction coefficient distribution.

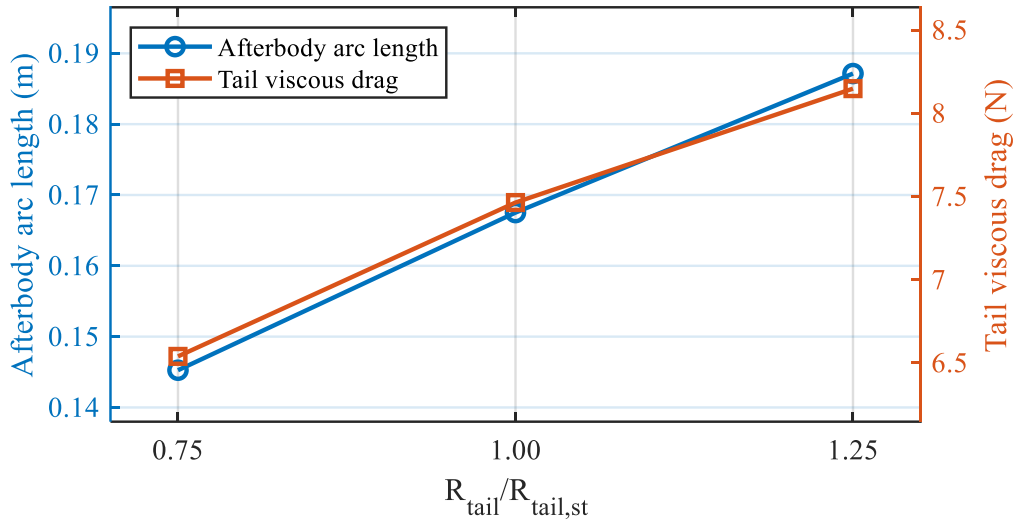



Figure 8 – Relation between afterbody arc length and tail viscous drag.

Table 2 – Afterbody arc length and skin-friction indicators for three tail-curvature cases at $Ma_\infty=6$.

| $R_{tail}/R_{tail,st}$ | Afterbody arc length (m) | Afterbody $\overline{C_f}$ | Afterbody $I_f$ | Tail viscous drag (N) |
|---|---|---|---|---|
| 0.75 | 0.1453 | $9.83\times10^{-4}$ | $1.43\times10^{-4}$ | 6.54 |
| 1.00 | 0.1675 | $9.69\times10^{-4}$ | $1.62\times10^{-4}$ | 7.46 |
| 1.25 | 0.1871 | $9.45\times10^{-4}$ | $1.77\times10^{-4}$ | 8.15 |

## 3.5 Entropy-Production Response and Regional Loss Decomposition

The entropy-production contours for the three curvature cases are compared in Fig. 9. The entropy-production contours exhibit similar spatial patterns, with high-entropy regions remaining in the shock-affected region, the afterbody boundary layer, and the near wake. This indicates that the tested curvature variation does not fundamentally change the topology of the major loss-generation regions at $Ma_\infty=6$. Instead, it modifies the intensity of entropy production. This intensity modulation is reflected in the integrated loss.

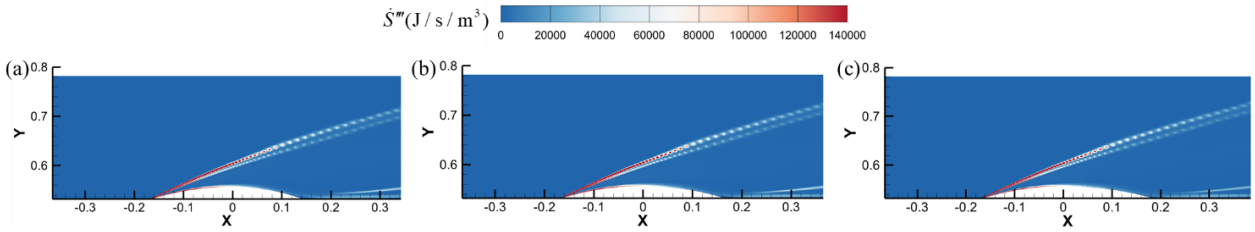



Figure 9 – Entropy-production contours for the three tail-curvature cases under $Ma_\infty = 6$: (a) $R_{tail} / R_{tail,st} = 0.75$; (b) $R_{tail} / R_{tail,st} = 1$; (c) $R_{tail} / R_{tail,st} = 1.25$.

The geometric regional integration is summarized in Table 3. The afterbody-neighborhood loss remains a small fraction of the whole-field loss, approximately 3.7-4.3% across the three curvature cases. This confirms that at $Ma_\infty = 6$, the global entropy-production loss is dominated by the forebody/shock-dominated region, while the afterbody contributes a smaller local portion. Nevertheless, the afterbody-neighborhood loss still varies with curvature, from 12.47 kJ/s for $R_{tail} / R_{tail,st} = 0.75$ to 14.51 kJ/s for the standard case and 13.55 kJ/s for $R_{tail} / R_{tail,st} = 1.25$.

Table 3 – Entropy-production loss of three tail-curvature cases under $Ma_\infty = 6$.

| $R_{tail} / R_{tail,st}$ | Region | Thermal loss (kJ/s) | Viscous loss (kJ/s) | Total loss (kJ/s) |
|---|---|---|---|---|
| 0.75 | Forebody-dominated | 89.12 | 194.61 | 283.73 |
| | Afterbody-neighborhood | 7.04 | 5.43 | 12.47 |
| | Whole field | 96.16 | 200.04 | 296.20 |
| 1.00 | Forebody-dominated | 118.17 | 255.19 | 373.36 |
| | Afterbody-neighborhood | 8.21 | 6.30 | 14.51 |
| | Whole field | 126.38 | 264.49 | 387.87 |
| 1.25 | Forebody-dominated | 93.41 | 205.15 | 298.56 |
| | Afterbody-neighborhood | 8.11 | 5.44 | 13.55 |
| | Whole field | 101.52 | 210.59 | 312.11 |

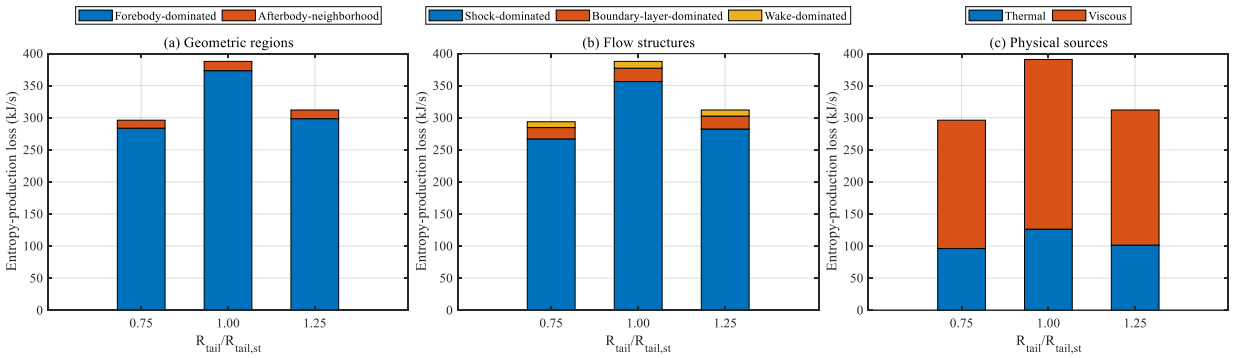



Figure 10 – Entropy-production loss decomposition: (a) regional loss by geometric region; (b) loss by flow structure; (c) thermal/viscous contribution.

As shown in Fig. 10(b), the shock-dominated region contributes approximately 90–92% of the total entropy-production loss for all three curvature cases, whereas the boundary-layer-dominated and wake-dominated contributions are much smaller. This confirms that the present $Ma_\infty = 6$ condition is globally shock-dominated.

Relative to the standard ($R_{tail} / R_{tail,st} = 1$) case, the afterbody loss decreases by 14.1% at $R_{tail} / R_{tail,st} = 0.75$ and 6.6% at $R_{tail} / R_{tail,st} = 1.25$, while the whole-field loss decreases by 23.6% and 19.5%, respectively. Notably, the afterbody contribution remains a small but consistent fraction of the total, about 3.7-4.3% across all three cases, which supports the visual observation that curvature mainly scales the local irreversibility level. A plausible interpretation is that, since the forebody and main-body geometry are fixed, the overall compression and boundary-layer/wake structure remain largely constrained, so the primary entropy-production regions remain in the same places. Changing $R_{tail}$ modifies the local

pressure recovery and near-wall gradients around the afterbody, which can strengthen or weaken entropy production without relocating it; the non-monotonic trend suggests an intermediate curvature may produce the strongest combined effect of compression and shear in this profile.

The entropy-production trend is broadly consistent with the force-based drag result in identifying the standard curvature case as the most loss-intensive among the three cases. The standard case has the largest total drag, 239.34 N, and the largest whole-field entropy-production loss, 387.87 kJ/s. However, the ranking of the other two curvature cases is not strictly identical between drag and entropy production. A strict one-to-one correspondence is not expected, which is physically reasonable because drag is a directional surface-force quantity, whereas entropy production is a scalar measure of irreversible loss generation.

From this perspective, the entropy-production analysis provides two important insights. First, the afterbody-neighborhood loss is small compared with the whole-field loss at $Ma_\infty = 6$, which explains the weak sensitivity of total drag and total entropy loss to moderate afterbody curvature variation. Second, the afterbody remains a physically important region because pressure recovery, boundary-layer development, wake formation, and shock-affected near-wall gradients can overlap there. Even when the integrated afterbody-neighborhood loss is small, local entropy-production intensity can still change and may be linked to curvature-induced changes in drag components, as illustrated in Fig. 10.

## 4. Conclusions and Outlook

Analysis of afterbody-curvature-induced drag and loss characteristics has been conducted for a two-dimensional wide-range-speed aircraft profile. The main conclusions are as follows.

First, the afterbody-curvature study shows that the total drag is only weakly affected by moderate changes in $R_{tail}$. From $R_{tail} / R_{tail,st} = 0.75$ to 1.25, the net total drag decreases by only about 0.39%.

However, this weak total response hides a clear redistribution between pressure and viscous drag. The net pressure drag decreases by approximately 1.31%, while the net viscous drag increases by approximately 4.32%.

Second, the tail-region decomposition shows the curvature-induced mechanism more clearly. As $R_{tail} / R_{tail,st}$ increases from 0.75 to 1.25, the tail pressure drag decreases by 9.82%, whereas the tail viscous drag increases by 24.61%. The tail total drag decreases by only 3.07%, indicating a strong compensation between the pressure and viscous contributions.

Third, surface-pressure and skin-friction distributions clarify the physical origin of this compensation. The $C_p$ distribution indicates that afterbody curvature modifies the pressure-recovery process and, together with the changed surface orientation, reduces the pressure-drag contribution. The $C_f$ distribution shows that the local skin-friction level does not increase with $R_{tail}$. Instead, the afterbody arc length increases, leading to a larger integrated viscous contribution. Therefore, the viscous-drag increase is mainly associated with the larger afterbody surface length rather than local wall-shear intensification.

Finally, entropy-production analysis shows that the main high-entropy regions remain in similar locations across the three curvature cases, while their intensity changes with $R_{tail}$. The afterbody-neighborhood loss accounts for only about 3.7-4.3% of the whole-field loss at $Ma_\infty = 6$, and the shock-dominated region contributes approximately 90-92% of the total entropy-production loss. This explains why the global response to curvature is modest under the present hypersonic condition. Nevertheless, entropy production remains useful for identifying how curvature affects local irreversibility intensity and for interpreting the loss-generating mechanism near the afterbody.

Overall, afterbody curvature affects drag through coupled and competing pressure and viscous pathways. A curvature change that reduces pressure drag may simultaneously increase viscous drag because of the longer afterbody surface. Therefore, curvature-aware afterbody design should consider not only total drag, but also pressure/viscous drag decomposition and local irreversibility generation.

Future work will focus on wind-tunnel experiments to further examine the detailed flow structures in the afterbody and near-wake regions. In particular, flow visualization and quantitative measurements will be used to investigate the evolution of the afterbody boundary layer, the wake development, and the local interaction between compression waves, shear layers, and near-wall

viscous effects. These experimental observations will help validate the present numerical interpretation and provide a more detailed physical basis for understanding the local loss-generation mechanism induced by afterbody curvature.

## 5. Contact Author Email Address

Corresponding Author: Dr. Miaosheng He.

Email Address: hms880912@sjtu.edu.cn.

## 6. Copyright Statement

The authors confirm that they, and/or their company or organization, hold copyright on all of the original material included in this paper. The authors also confirm that they have obtained permission, from the copyright holder of any third party material included in this paper, to publish it as part of their paper. The authors confirm that they give permission, or have obtained permission from the copyright holder of this paper, for the publication and distribution of this paper as part of the ICAS proceedings or as individual off-prints from the proceedings.

## References


[1] Shrewsbury G D. Effect of boattail juncture shape on pressure drag coefficients of isolated afterbodies. NASA TM X-1517, 1968.

[2] Silhan F V and Cubbage J M Jr. Drag of conical and circular-arc boattail afterbodies at Mach numbers from 0.6 to 1.3. NACA RM L56K22, 1957.

[3] Pendergraft O C Jr, Burley J R II and Bare E A. Parametric study of afterbody/nozzle drag on twin two-dimensional convergent-divergent nozzles at Mach numbers from 0.60 to 1.20. NASA Technical Paper 2640, 1986.

[4] Deere K A and Hunter C A. Experimental investigation of convoluted contouring for aircraft afterbody drag reduction. *35th AIAA/ASME/SAE/ASEE Joint Propulsion Conference and Exhibit*, AIAA Paper 99-2670, 1999.

[5] Naterer G F and Camberos J A. Entropy and the second law fluid flow and heat transfer simulation. *Journal of Thermophysics and Heat Transfer*, Vol. 17, No. 3, pp. 360-371, 2003.

[6] Zhou L, Hang J, Bai L et al. Application of entropy production theory for energy losses and other investigation in pumps and turbines: A review. *Applied Energy*, Vol. 318, Article 119211, 2022.

[7] Lin D, Yuan X and Su X. Local entropy generation in compressible flow through a high-pressure turbine with delayed detached eddy simulation. *Entropy*, Vol. 19, No. 1, Article 29, 2017.

[8] Moore J and Moore J G. Entropy production rates from viscous flow calculations: Part I: A turbulent boundary-layer flow. *ASME Paper*, 83-GT-70, 1983.

[9] Greitzer E M, Tan C S and Graf M B. *Internal flow: Concepts and applications*. Cambridge University Press, 2004.

[10] Xu Y. Method and application of detection of flow structures in supersonic flow with multiple wave interaction. PhD thesis, Tsinghua University, Beijing, 2016.